Sensors & Actuators: B. Chemical 423 (2025) 136732

Contents lists available at ScienceDirect

Sensors and Actuators: B. Chemical

journal homepage: www.elsevier.com/locate/snb

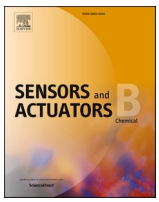

Chemiresistive room temperature H_2S sensor based on Cu_nO nanoflowers fabricated by laser ablation

Wenqing Zhao [a,b], Guanyu Yao [a,b], Hao Wu [b,c], Yadong Liu [a,b], Huichao Zhu [b,c], Zhengxing Huang [b,c], Wei Chen [d], Hongxu Liu [d], Xiaogan Li [b,e], Jingtong Na [a], Kairong Qin [a,b], Jun Yu [a,b,*]

[a] Central Hospital of Dalian University of Technology, Dalian 116024, PR China
[b] Key Lab of Liaoning for Integrated Circuits and Medical Electronic Systems, School of Biomedical Engineering, Dalian University of Technology, Dalian 116024, PR China
[c] School of Control Science and Engineering, Dalian University of Technology, Dalian 116024, PR China
[d] Cancer Hospital of Dalian University of Technology, Liaoning Cancer Hospital & Institute, Shenyang 110801, PR China
[e] School of Integrated Circuits, Dalian University of Technology, Dalian 116024, PR China

ARTICLE INFO

Key words:
Room-temperature H_2S sensor
Laser ablation
Cu_nO nanoflowers
PH

ABSTRACT

Hierarchical Cu_nO nanoflowers were synthesized through the laser ablation of a CuO target in NaOH solutions for room-temperature (27 °C) H_2S detection. Notably, the pH value of NaOH solutions influenced both the micro-morphologies and compositions of the Cu_nO products, as evidenced by XRD, XPS, SEM and TEM. In high pH solutions, the specific surface area of the Cu_nO products increased, their thickness decreased, and the Cu_2O content diminished, resulting in enhanced sensitivity, selectivity and stability of the Cu_nO products' response to H_2S. Notably, the pH14# sample synthesized using an NaOH solution with a pH value of 14 featured pure CuO nanoflowers comprising slightly curled nanosheets with a thickness of approximately 10 nm. This sensor demonstrated excellent H_2S sensing performance at room temperature, exhibiting a response value of 1.17 for 10 ppb H_2S, along with high selectivity and good long-term stability. However, after exposure to H_2S, the resistance of the sensor did not recover to its baseline in air at room temperature. Thermogravimetry results revealed that a temperature of 300 °C was effective for recovery of the sensor. Consequently, the operation temperature of the pH14# sensor was controlled using a micro-hotplate. In the pulse heating mode, the sensor's response to 100 ppb H_2S was 1.5, with a response time of 135 s and a recovery time of 137 s.

1. Introduction

H_2S is extensively employed across diverse sectors, including agriculture [1], manufacturing [2], and the oil and gas industries [3]. However, H_2S is a hazardous, corrosive, and flammable substance with a distinctive rotten egg odor [4]. Consequently, the acceptable ambient levels of H_2S, as recommended by the Scientific Advisory Board on Toxic Air Pollutants, are limited to 20–100 ppb [5,6]. In addition to its applications, H_2S also serves as a valuable trace biomarker for the early diagnosis of oral [7], digestive tract [8], and lung [9] diseases and is recognized as a key endogenous gas transmitter in pathophysiological processes [10]. Hence, developing sensors capable of detecting sub-ppm H_2S in vicinity of public and human breath is essential.

To date, several kinds of sensors capable of detecting low concentrations of H_2S have been introduced, including electrochemical sensors [11], fluorescent probes [12], acoustic wave sensors [13], optical waveguide sensors [14] and metal-oxide-semiconductor (MOS) sensors [15,16]. Among these, MOS sensors have garnered significant research attention owing to their low cost, ease of production, and excellent portability. Consequently, MOS sensors employing diverse semiconductor materials, such as SnO_2 [17], ZnO [18], CuO [19], Fe_2O_3 [20], WO_3 [21], and MoO_3 [22], have been developed. Among these materials, CuO-based nanomaterials have become particularly prominent owing to the exceptional adsorption capacity and high chemical affinity of CuO for H_2S [23,24]. Several recent studies have proposed and developed various types of CuO nanomaterials [19,25–27]. Among these, hierarchical and low-dimensional CuO nanostructures have been reported to demonstrate particularly desirable characteristics for H_2S

* Corresponding author at: Central Hospital of Dalian University of Technology, Dalian 116024, PR China.
E-mail address: junyu@dlut.edu.cn (J. Yu).

https://doi.org/10.1016/j.snb.2024.136732
Received 13 May 2024; Received in revised form 29 September 2024; Accepted 1 October 2024
Available online 3 October 2024

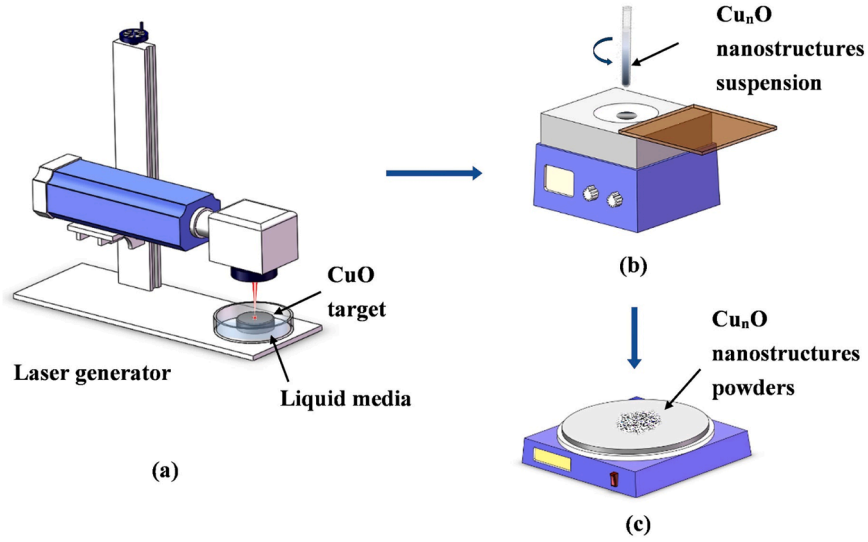

Fig. 1. Synthesis procedure for the Cu$_n$O samples: (a) ablation treatment, (b) centrifugation, and (c) drying.

sensing, including rapid responses, room temperature operation, low detection limits, and excellent conductivity [19,26–28]. However, the non-recovery response or long response time of room-temperature sensors severely inhibit their practical applications [29].

Among the various methods commonly adopted for synthesizing CuO nanostructures, laser ablation stands out as an economical, efficient, and straightforward technique, known to produce a diverse range of oxide nanostructures [30]. Furthermore, with the selection of appropriate targets and liquids with suitable properties, laser ablation can facilitate the controlled synthesis of various nanomaterials. In this context, one key factor influencing the morphology of nanoparticles is the pH value of the utilized liquid. Hyeon et al. synthesized Cu/Cu_2O/CuO nanoparticles, nanospindles, and nanoflowers through the laser ablation of a Cu target in de-ionized water and different concentration of NaOH solution. This report revealed that the pH value of the solution influenced both the composition and morphology of the synthesized nanoparticles [31]. Zhang et al. reported that reducing the pH value of the solution below 1.0 resulted in the formation of quasi-spheres comprising several WO_3 nanoplates [32]. Despite solid evidence suggesting the influence of solution pH on the morphologies of CuO nanoparticles, a comprehensive understanding of the underlying influence mechanism remains elusive. Furthermore, the specific correlation between the solution pH and gas-sensing performance of products remains unknown. Notably, compared to a Cu target, a CuO target theoretically absorbs laser energy more efficiently, making it a suitable choice for synthesizing gas-sensing materials in this study.

This paper reports the fabrication of hierarchical Cu$_n$O nanoflowers through the laser ablation of CuO targets in NaOH solutions. Furthermore, it details a systematic analysis of H_2S sensing performance of these nanoflowers. Moreover, the paper discusses the growth mechanism of the hierarchical Cu$_n$O nanoflowers based on their micro-structure and chemical composition. It also highlights the significant impact of OH^- ions on H_2S sensing performance of the Cu$_n$O products.

2. Experimental section

2.1. Materials

Copper oxide target (5 mm thick, purity quotient ≥99.9 %, CuO) and sodium hydroxide (purity quotient ≥96 %, NaOH) were purchased from Deyang ONA New Materials corporation and Tianjin Tianli Chemical Reagents corporation, respectively. All chemical reagents utilized in this study were of analytical grade and used without further purification.

2.2. Preparation of Cu$_n$O samples

Fig. 1 illustrates the synthesis procedure for the Cu$_n$O samples. First, a CuO target was immersed in appropriate liquids with a depth of 8 mm. The liquid media included pure water or NaOH solutions with pH values of 6.5 (pure water) 8, 10, 12, or 14. The resulting Cu$_n$O products were respectively labeled as pw$^{\#}$, pH8$^{\#}$, pH10$^{\#}$, pH12$^{\#}$, and pH14$^{\#}$. A nanosecond-pulsed fiber laser (Wuxi Raycus Fiber Laser Technologies Co., Ltd.) with a central wavelength of 1064 ± 4 nm, pulse width of 131 ns, and frequency of 20 kHz was employed in this study. The laser beam scanned a square area of 7 mm × 7 mm on the surface of the CuO target, moving at a speed of 2 mm/s over an irradiation time of 8 min. As the laser spot moved, it continuously ablated a specific surface area of the CuO target, generating Cu$_n$O nanostructures subsequently dispersed into the liquid, as depicted in Fig. 1(a). The suspension was then collected and centrifuged at 6000 rpm, following which the precipitate was washed with deionized water and subsequently dried at 70 °C to obtain Cu$_n$O powder samples, as depicted in Fig. 1(b) and (c). Finally, all Cu$_n$O samples were annealed at 600 °C for 1 h in a muffle furnace.

2.3. Characterization of materials

The surface morphologies and internal structures of the as-prepared Cu$_n$O samples were examined using field-emission scanning electron microscopy (FE-SEM, JSM-7610 Plus, JEOL) and transmission electron microscopy (TEM, FEI Talos F200X G2, Thermo Fisher Scientific), respectively. The crystalline phase was analyzed by X-ray diffraction (XRD, Dmax Ultima IV, Rigaku) equipped with a Cu Kα radiation source (λ = 0.15418 nm). The chemical states of Cu and O were examined using X-ray photoelectron spectroscopy (XPS, Thermo Kalpha, Thermo Fisher Scientific) with a monochromatic Al Kα X-ray source. Furthermore, thermogravimetry (TG) and differential thermogravimetry (DTG) analyses were performed using a thermogravimetric analyzer (TGA, TGA 550, TA Instruments). Additionally, minimal weight changes of the samples during H_2S sensing were measured using another TGA (LoC-TGA-1001, Xiamen High-End MEMS Technology Co., Ltd.). The specific surface areas were estimated using the Brunauer–Emmett–Teller (BET) method (Micromeritics ASAP 2460 3.01) based on nitrogen adsorption–desorption experiments.

2.4. Gas sensors fabrication

To achieve low power consumption (Figure S1) and precise control

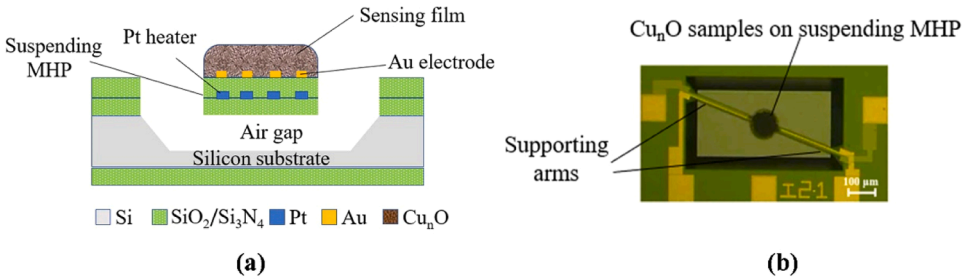

Fig. 2. (a) Schematic sideview of the fabricated gas sensor. (b) Top-view image of the Cu_nO sensor.

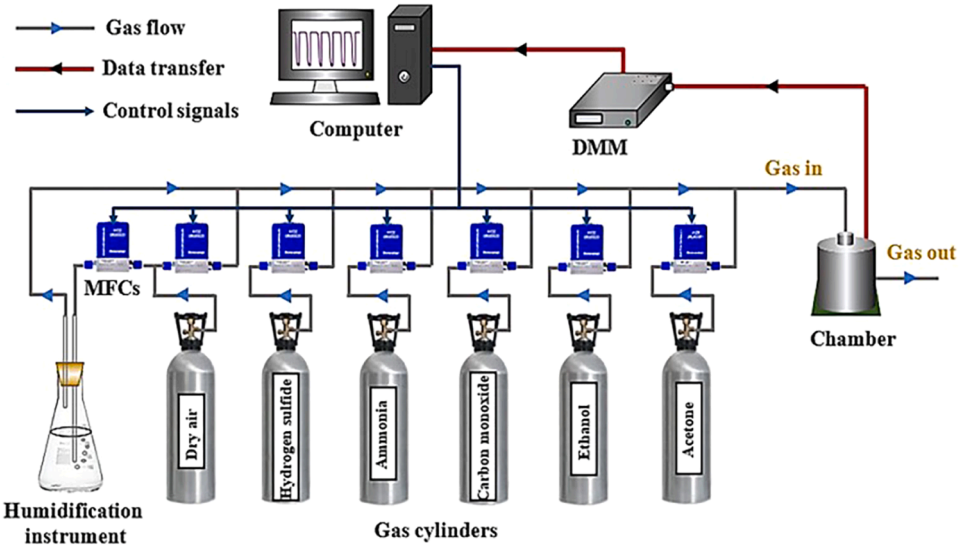

Fig. 3. Schematic of the gas measurement system.

over the operating temperature, Cu_nO samples were coated onto micro-heater plates (MHPs) [33,34] comprising Pt heater strips and Au electrodes embedded within an SiO_2/Si_3N_4 membrane, as illustrated in Fig. 2(a). Initially, Cu_nO pulp samples were prepared as follows: A dispersing agent (DS-901, Tianjin Surfy Chem T&D Co., Ltd.) was added to 5 ml deionized water to create a 12.5 % dispersant solution. Subsequently, the Cu_nO samples were ground and dispersed in this dispersant at a concentration of 5 wt%. A high-precision electrohydrodynamics inkjet printer (RD-EHD 200, shanghai Ruidu Photoelectric Technology Co., Ltd.) was then utilized to spray the resulting Cu_nO pulp samples onto the Au electrodes of the MHPs, as illustrated in Fig. 2(b). Finally, all fabricated Cu_nO sensors were heated to 300 °C for 2 h to eliminate the dispersing agent from the pulp samples.

2.5. Gas sensing measurement

A dynamic gas sensing measurement method was adopted for this experiment, as illustrated in Fig. 3. The measurement system included standard gas cylinders (Dalian Guangming Special Gas Products Co., Ltd.), mass flow controllers (MFCs) driven by a computer system, a sealed chamber for the fabricated Cu_nO sensors and a temperature and humidity sensor (SHT31-ARP, Sensirion). A humidification instrument and a digital multimeter (DMM) for data collection were also included. During the measurement process, relative humidity (RH) was controlled by mixing wet and dry air in specific proportions and was monitored by the temperature and humidity sensor. Furthermore, the concentration of the test gas was adjusted by mixing the test gas with air in a predetermined proportion.

The resistances of the gas sensor in air and in the test gas atmosphere

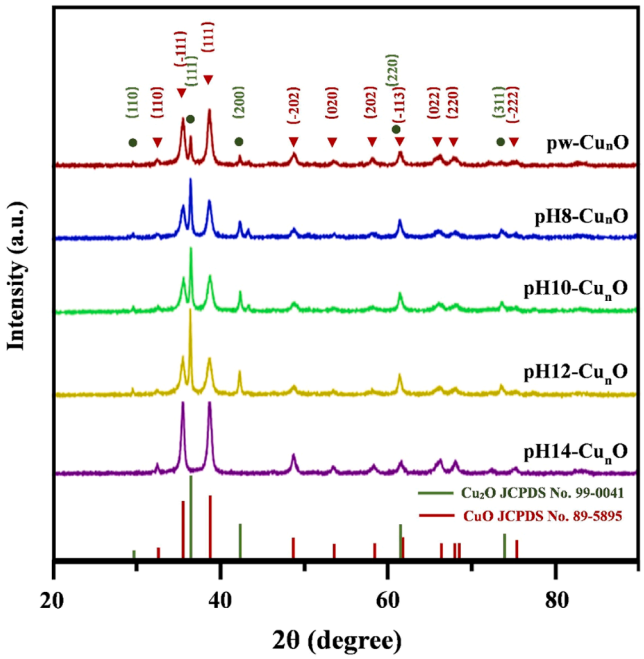

Fig. 4. XRD patterns of the Cu_nO samples.

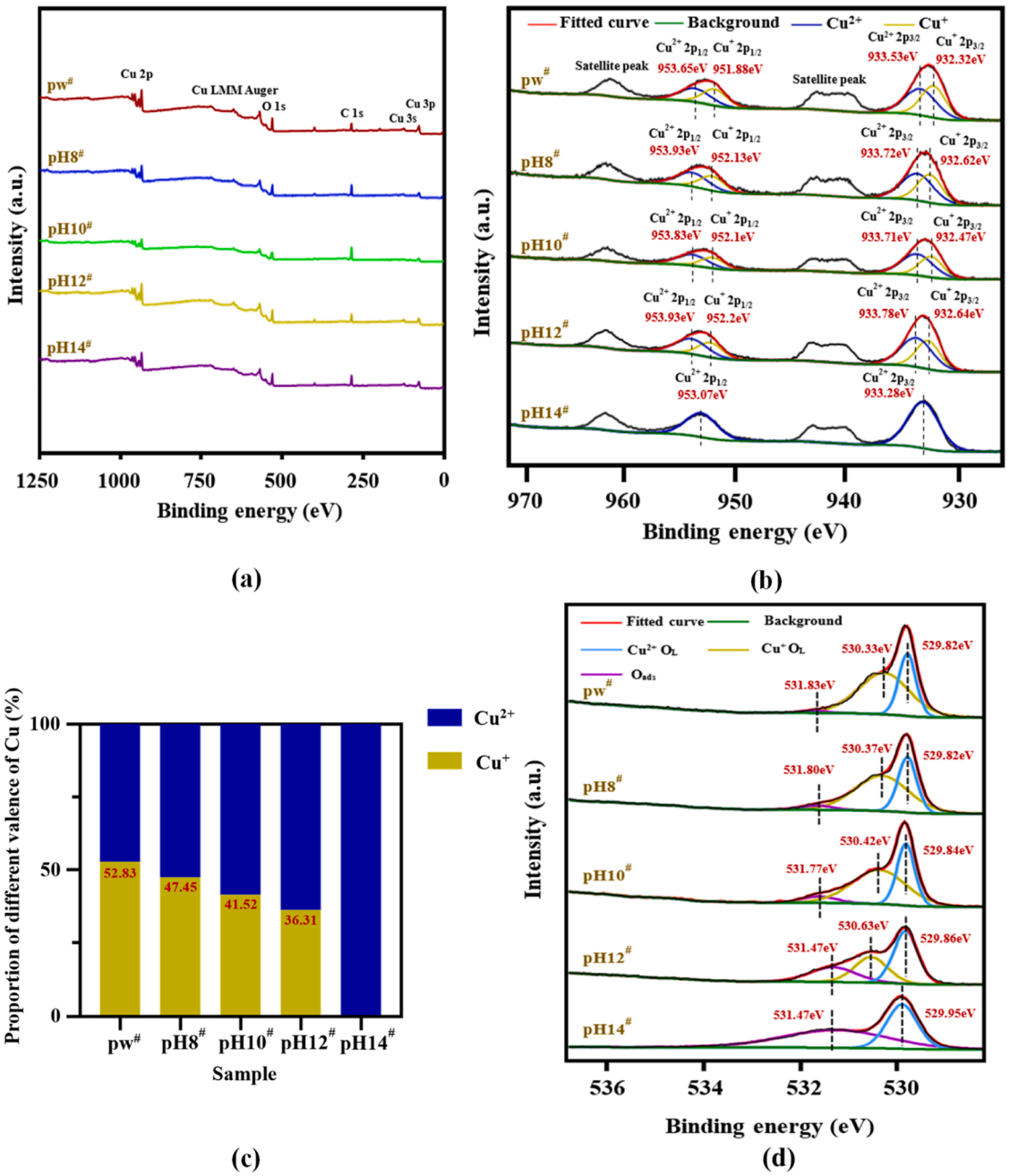

Fig. 5. XPS spectra of the Cu_nO samples: (a) survey spectra and (b) Cu 2p spectra. (c) Proportion of different Cu valences. (d) O 1 s spectra.

were defined as R_a and R_g, respectively, while the sensor response was calculated as $S = R_g/R_a$. The response time was defined as the duration required for the resistance to change by 90 % after exposure to the test gas [35].

3. Results and discussion

3.1. XRD, XPS, SEM, TEM, BET analysis

The phases and crystallinity of the as-prepared Cu_nO samples were examined based on the XRD patterns illustrated in Fig. 4. Notably, the XRD curves of pw#, pH8#, pH10#, and pH12# correspond to the monoclinic CuO (JCPDS No. 89–5895) and cubic Cu_2O phases (JCPDS No. 99–0041). However, the XRD pattern of pH14# displays no prominent diffraction peaks corresponding to Cu_2O phases but exclusively aligns with the monoclinic CuO.

The elemental chemical states of the as-prepared Cu_nO samples were characterized based on the XPS spectra depicted in Fig. 5. Notably, the survey spectrum of each sample displayed in Fig. 5(a) clearly reveals peaks corresponding to O, Cu, and C. Fig. 5(b) illustrates the Cu 2p spectra of the samples. Here, the peaks in the spectrum of the pw#, pH8#, pH10#, and pH12# samples are attributed to both Cu^{2+} and Cu^{+}. However, the spectrum of pH14# exclusively displays peaks corresponding to Cu^{2+}, aligning with the XRD result. Fig. 5(c) reveals that the proportion of Cu^{+} decreased from 52.83 % to 0 as the pH value of the solution increased from 6.5 to 14, derived from Cu 2p spectra in Fig. 5 (b). Fig. 5(d) displays the O 1 s spectra of the samples, displaying two peaks in the spectrum of pH14# and three peaks in the spectra of pw#, pH8#, pH10#, and pH12#. Notably, the two peaks in the spectrum of pH14# are located at 529.95 eV and 531.47 eV, originating from the lattice oxygen (O_L) of CuO and surface-adsorbed oxygen (O_{ads}) [36,37]. The spectra of the other samples display a peak centered at

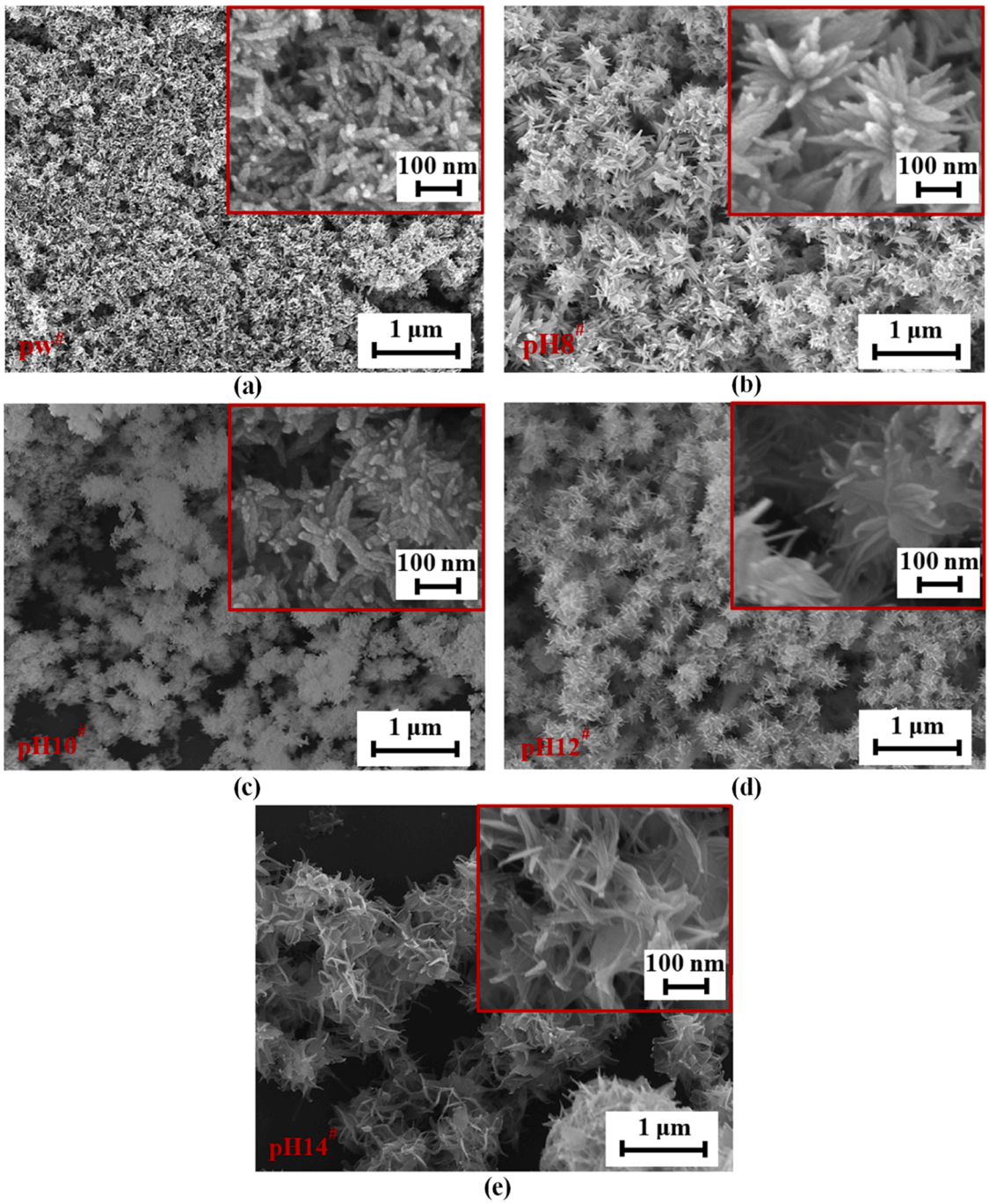

Fig. 6. SEM images of the Cu_nO samples: (a) pw#, (b) pH8#, (c) pH10#, (d) pH12#, and (e) pH14#.

approximately 530.5 eV, which is attributed to the lattice oxygen of Cu_2O [38]. Notably, the ratio of peak area of surface adsorbed oxygen to lattice oxygen rises with the increase of pH, which suggests the samples fabricated in high pH solution have advantage to surface-adsorb more oxygen.

The SEM images reveal that the pH value of the utilized liquid medium significantly influenced the morphologies of the Cu_nO products. As illustrated in Fig. 6(a), the Cu_nO product (pw#) obtained in pure water primarily comprised densely stacked spindle-shaped particles, approximately 100 nm in length, exhibiting minimal aggregation. However, when CuO targets are ablated in NaOH solutions, the major products were hierarchical nanoflowers. The petals of these nanoflowers gradually stretched and underwent thinning with increasing pH, as illustrated in Fig. 6(b—e). Notably, the micro-morphology of the pH14# sample exhibited dramatic changes, as depicted in Fig. 6(e). Here, the petals enlarged and curled, thus interconnecting with each other, moreover, their thickness reduced to approximately 10 nm. These changes result in a more loose and porous structure of pH14#, theoretically providing a large specific surface area, which can enhance gas diffusion and adsorption during gas sensing.

TEM observations further validate the results of the XRD, XPS, and SEM analysis, including the polycrystalline structure, components, and morphologies of the Cu_nO samples. Fig. 7(a) illustrates that the crystal planes of both monoclinic CuO and cubic Cu_2O are apparent at the top (IV of Fig. 7(a)) and root (III of Fig. 7(a)) of a petal formed in pw#. However, for nanoflowers fabricated in NaOH solutions, the crystal planes of cubic Cu_2O are rarely observed at top of the petals (IV of Fig. 7 (b—d) and in thin areas (III and IV of Fig. 7(e)), where Cu_2O interacts

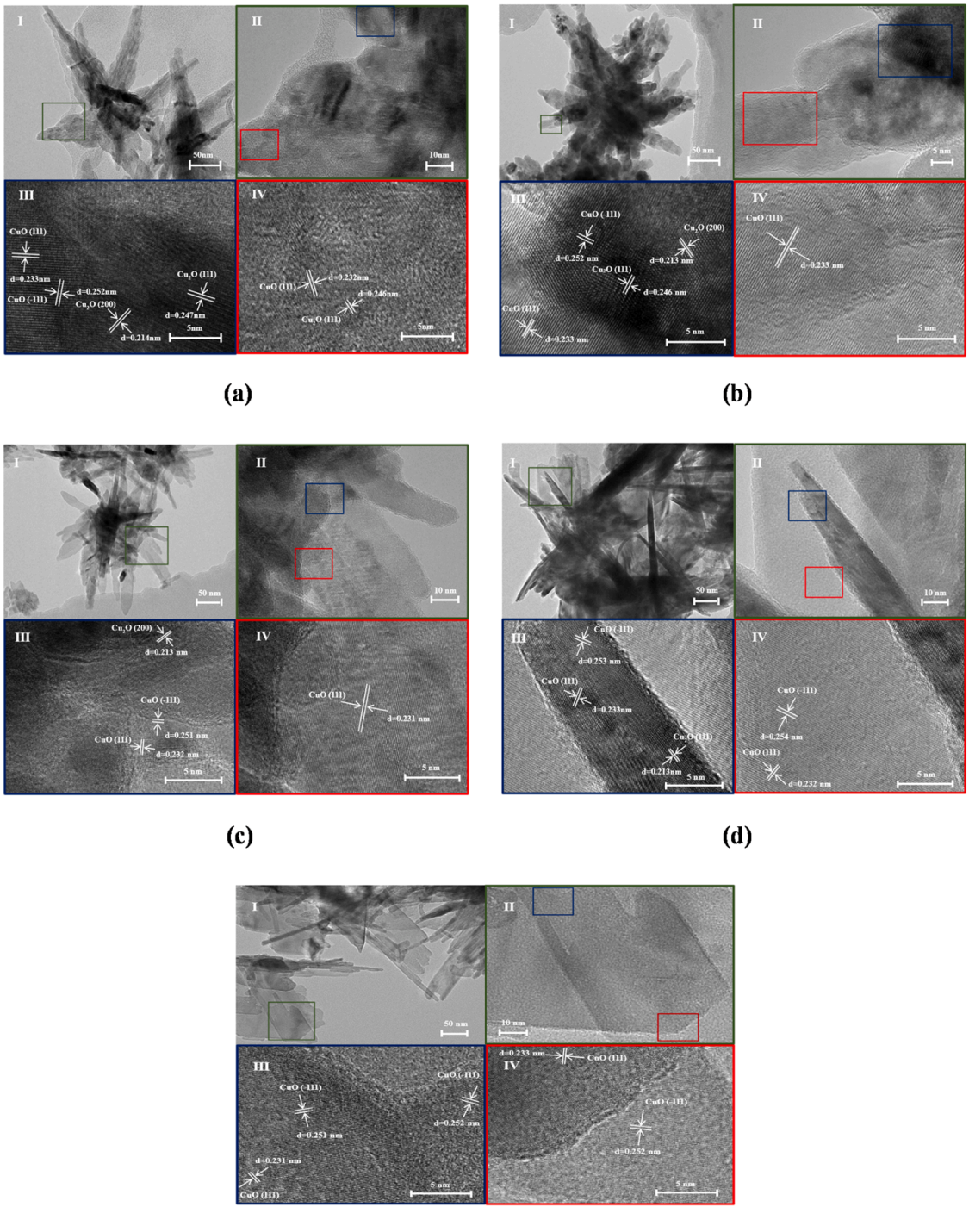

Fig. 7. TEM images of the Cu_nO samples (a) pw#, (b) pH8#, (c) pH10#, (d) pH12#, and (e) pH14#. (Images with colored borders depict magnified views of scenes highlighted using small frames of the same color.).

more readily with NaOH compared to other areas.

The BET method was used to measure the nitrogen adsorption–desorption isotherms to study the specific surface areas of the Cu_nO samples, as illustrated in Fig. 8. Notably, the specific surface area of pw#, pH8#, pH10#, pH12#, and pH14# were determined to be 4.57, 10.41, 18.84, 23.94, and 30.83 m^2/g, respectively. Thus, compared to the pw# sample featuring nanospindles, the pH10#, pH12#, and pH14# samples featuring nanoflowers exhibited large specific surface area. The specific surface area of sample enlarged as pH value increased. The increasing specific surface area further increased the number of active sites available for gas adsorption, as evidenced by the O 1 s spectra depicted in Fig. 5(d), and are anticipated to improve the gas sensitivity of the samples.

3.2. Gas sensing performance

Fig. 9(a) presents the response curves of the Cu_nO sensors. Notably, when these sensors were exposed to H_2S at room temperature, their

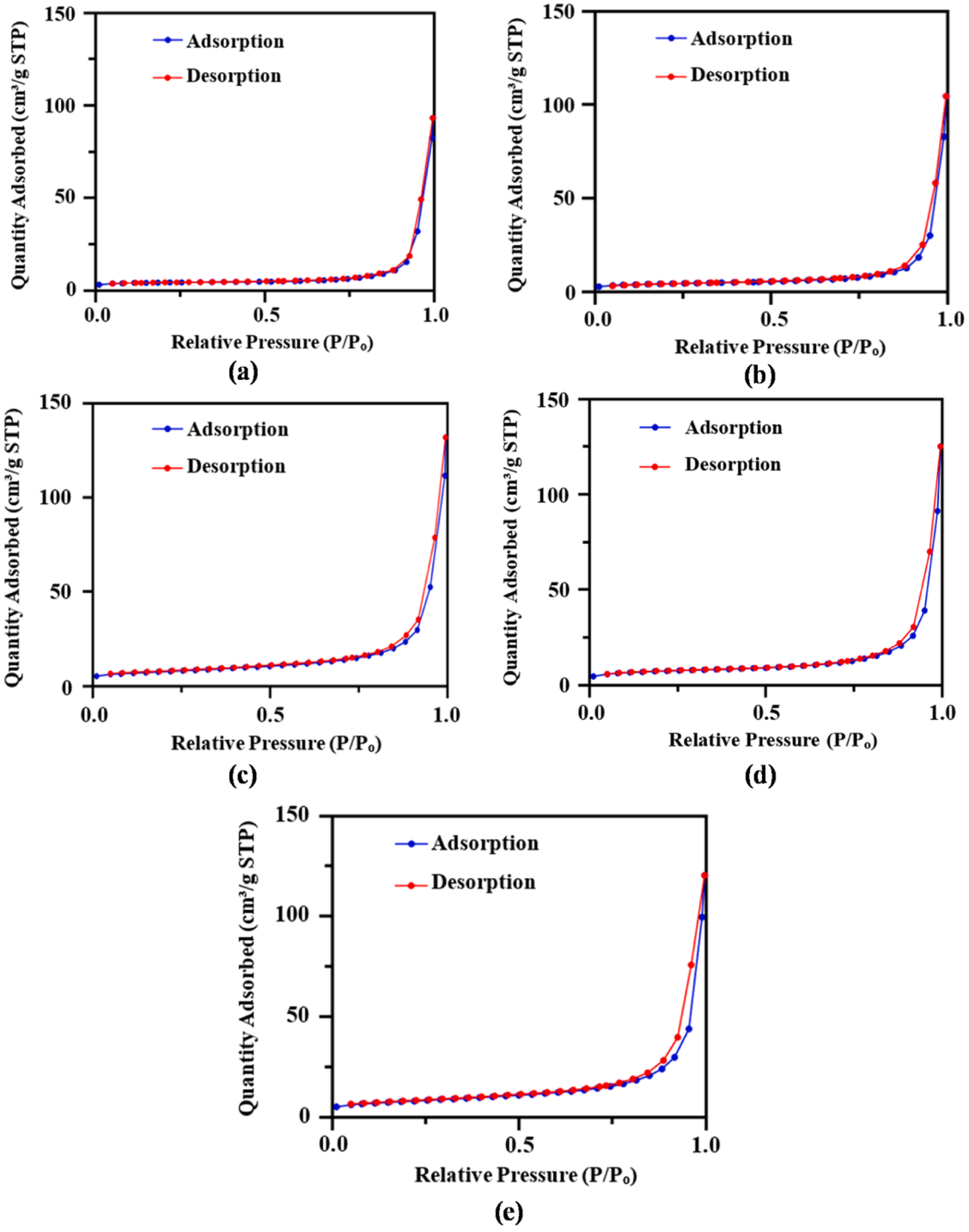

Fig. 8. Nitrogen adsorption–desorption isotherms for (a) pw$^{\#}$, (b) pH8$^{\#}$, (c) pH10$^{\#}$, (d) pH12$^{\#}$, and (e) pH14$^{\#}$.

resistances increased, indicating p-type semiconductor characteristics. However, when the sensors were exposed to air again, their resistance did not entirely recover to the original value in air (R_a) at room temperature (Figure S2). To expedite H_2S desorption from the sensing materials, the sensors were heated to 300 °C. This treatment lowered their resistances below R_a, owing to increased carrier concentrations. After heating, the sensors were allowed to cool to room temperature. Then their resistances recovered to R_a, signifying successful H_2S desorption.

Fig. 9(b) displays the response values and response times of the Cu_nO sensors. While the pw$^{\#}$ sample exhibited no response to H_2S, the pH8$^{\#}$, pH10$^{\#}$, pH12$^{\#}$, and pH14$^{\#}$ samples (featuring Cu_nO nanoflowers) exhibited varying degrees of sensitivity to 10 ppm H_2S at room temperature. As the pH increased from 8 to 14, the response value of the sensors increased from 2.075 to 208.91, while their response time decreased progressively.

The response of the Cu_nO sensors to 10 ppm H_2S was tested over five cycles. The results reveal that all sensors exhibited good repeatability, with deviations within 6.84 %, as illustrated in Fig. 10 (a). To examine the selectivity of the Cu_nO sensors, their responses to 100 ppm CO, NH_3, C_2H_5OH, and CH_3COCH_3 and 10 ppm H_2S and NO_2 were recorded. Fig. 10 (b) shows that Cu_nO nanoflowers (pH8$^{\#}$, pH10$^{\#}$, pH12$^{\#}$, and pH14$^{\#}$) sensors responded much higher to H_2S than that of other gases

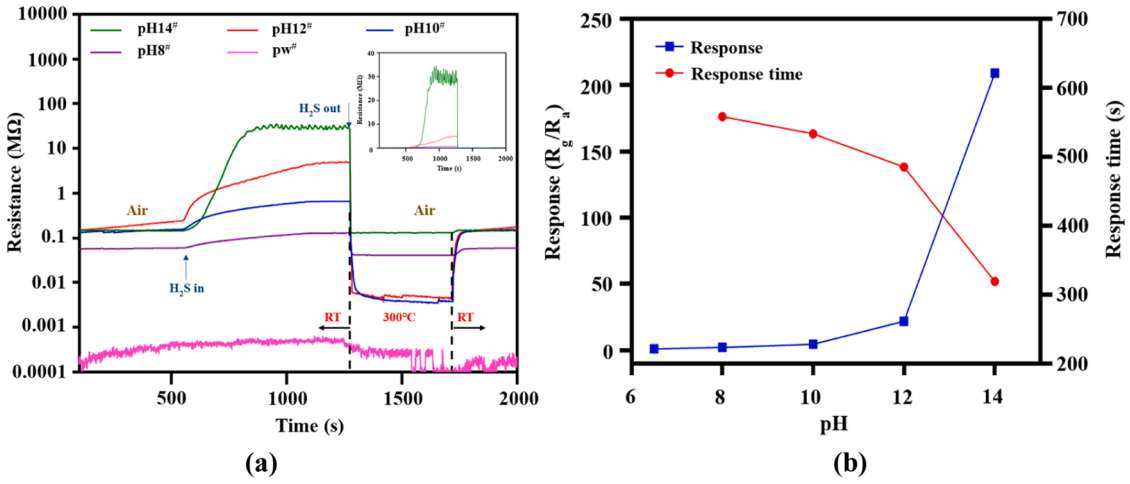

Fig. 9. (a) Response curves of the Cu_nO sensors to 10 ppm H_2S in a logarithmic scale. The inset depicts the curves in a linear scale. (b) Response values and times of the Cu_nO sensors.

at room temperature. Concurrently, the resulting Cu_nO nanoflowers fabricated in solution with a high pH exhibited enhanced selectivity to H_2S. For instance, the ratio of 10 ppm H_2S's response value to 10 ppm NO_2's increased from 1.66 to 13.5 as the pH value increased from 8 to 14. This may be attributed to the pH-induced reduction in the Cu_2O proportion within Cu_nO nanoflowers, as shown in Fig. 5(c). At room temperature, compared to CuO, Cu_2O is more readily sulfonated owing to the weaker Cu–O bonds in its crystal structure [39], as evidenced by Figure S3. However, the metallic characteristics of the resulting Cu_2S inhibit the required resistance increase and weaken the response during H_2S sensing [40], leading to reduced sensitivity and selectivity of the Cu_nO nanoflower sensors to H_2S.

Fig. 10 (c) illustrates the response values of the Cu_nO sensors to 10 ppm H_2S at temperatures ranging from 27 °C (RT) to 360 °C. The results reveal that the pw# (Cu_nO nanospindles) sensor achieved optimal operating temperatures at 220 °C, while the pH8#, pH10#, pH12#, and pH14# (Cu_nO nanoflowers) sensors exhibited optimal responses to 10 ppm H_2S at room temperature. Notably, for the pH14# sensor, the relationship between response and temperature is described by the equations: $S = 10^{-0.0154T+2.704}$ and $\frac{dS}{dT} = -17.94 \times 10^{-0.0154T}$, as indicated by the logarithmic fitting curve depicted in Fig. 10 (c). As T=27℃, $\frac{dS}{dT} = 6.89$. Compared with the linear fit between response and concentration of H_2S at ppm-level (Fig. 11(c)), the effect of temperature variations around room temperature on sensor's response to 10 ppm H_2S is about − 403 ppb/℃. Fig. 10 (d) indicates that the baseline (R_a) of the Cu_nO nanoflowers sensors decreased with increasing temperature.

Fig. 10 (e) illustrates the long-term stability of the Cu_nO nanoflowers sensors. Notably, the response of pH14# sensor to 10 ppm H_2S remained around the initial value, exhibiting less than 8 % fluctuations over 42 days, while the response values of the pH8#, pH10#, and pH12# sensors consistently decreased. For example, the response value of the pH12# sensor to 10 ppm H_2S demonstrated a reduction of 68.5 % after 42 days. Additionally, the Cu_nO sensors' baselines (R_a) were recorded over 42 days. As observed in Fig. 10 (e), the pH8#, pH10# and pH12# sensors exhibited increase in baseline (R_a), likely owing to the chemical instability of Cu_2O [41], which led to the instability of sensors.

The above analysis indicates that the pH14# sensor demonstrated significant advantages in terms of sensitivity, response time, selectivity, and long-term stability. Hence, its detection limit and its responses to 10 ppm H_2S under different relative humidity (RH) conditions were further explored. Fig. 11 (a) and (b) illustrate the pH14# sensor exhibited excellent sensing performance even for ppb-level H_2S at room temperature. The H_2S detection limit is 10 ppb with response value of 1.17. The response of the pH14# sensor demonstrated good linear relationships with H_2S concentrations at ppm-level and sub-ppm-level. The corresponding fitted curves and equations are illustrated in Fig. 11 (c), with correlation coefficients of 0.9875 and 0.9912, respectively. The resistance of the pH14# sensor at room temperature was tested continuously across an RH range of 0–77 % RH, as depicted in Fig. 11 (d). Fig. 11 (e) indicates that the response value of pH14# to 10 ppm H_2S gradually decreased, while its baseline (R_a) increased with the increase of relative humidity. According to the linear fit in Fig. 11 (e), the pH14#'s response to 10 ppm H_2S decreased 1.439 with the increase of 1 % RH at room temperature. Compared with the linear fit between response and concentration of H_2S at ppm-level (Fig. 11(c)), the effect of RH variations around room temperature on pH14# sensor's response to 10 ppm H_2S is about − 84 ppb/%RH.

To improve the practicality of the fabricated sensors, the pH14# sensor was operated in a pulse heating mode. Fig. 12 (a) depicts the resistance curve of the pH14# sensor to 100 ppb H_2S using the heating pulse illustrated in Fig. 12 (b). In a heating cycle, the sensor was heated to 300 ℃ under high level voltage for 3 s and worked at room temperature for 25 s. The response curve obtained when using the resistance at the 24th s of each heating cycle as the room temperature resistance of the sensor is depicted as a black curve in Fig. 12 (a). The response curve indicates that pH14# sensor's response to 100 ppb H_2S was 1.5 under pulse heating, with a response time of 135 s and a recovery time of 137 s.

3.3. Growth mechanism of Cu_nO nanoflowers

3.3.1. TG and DTG analysis

The composition of the unannealed sample was significant to investigate the synthesis mechanism of Cu_nO nanoflowers, thus unannealed pH14# was subjected to a thermogravimetric analysis. Specifically, it was heated from room temperature to 800 °C at a heating rate of 10 °C/min in air atmosphere. The mass change of this sample during this process is illustrated in Fig. 13. The TG and DTG curves reveal two stages of mass loss. The initial mass loss appearing between 34.6 °C and 201.2 °C corresponds to the desorption of intercalated H_2O (including surface-adsorbed H_2O) generated between the ultrathin petals of pH14# [42]. The second mass loss observed from 201.2 °C to 332.5 °C is attributed to the dehydration of lattice OH^- groups of $Cu(OH)_2$ [43]. Finally, the weight of pH14# stabilized after heating over 600 °C.

3.3.2. Growth mechanism of Cu_nO nanoflowers

The TGA results shows the existence of copper hydroxide, suggesting that the CuO target particles participated in the ablation reaction in the form of ions [44]. The growth mechanism of Cu_nO nanoflowers

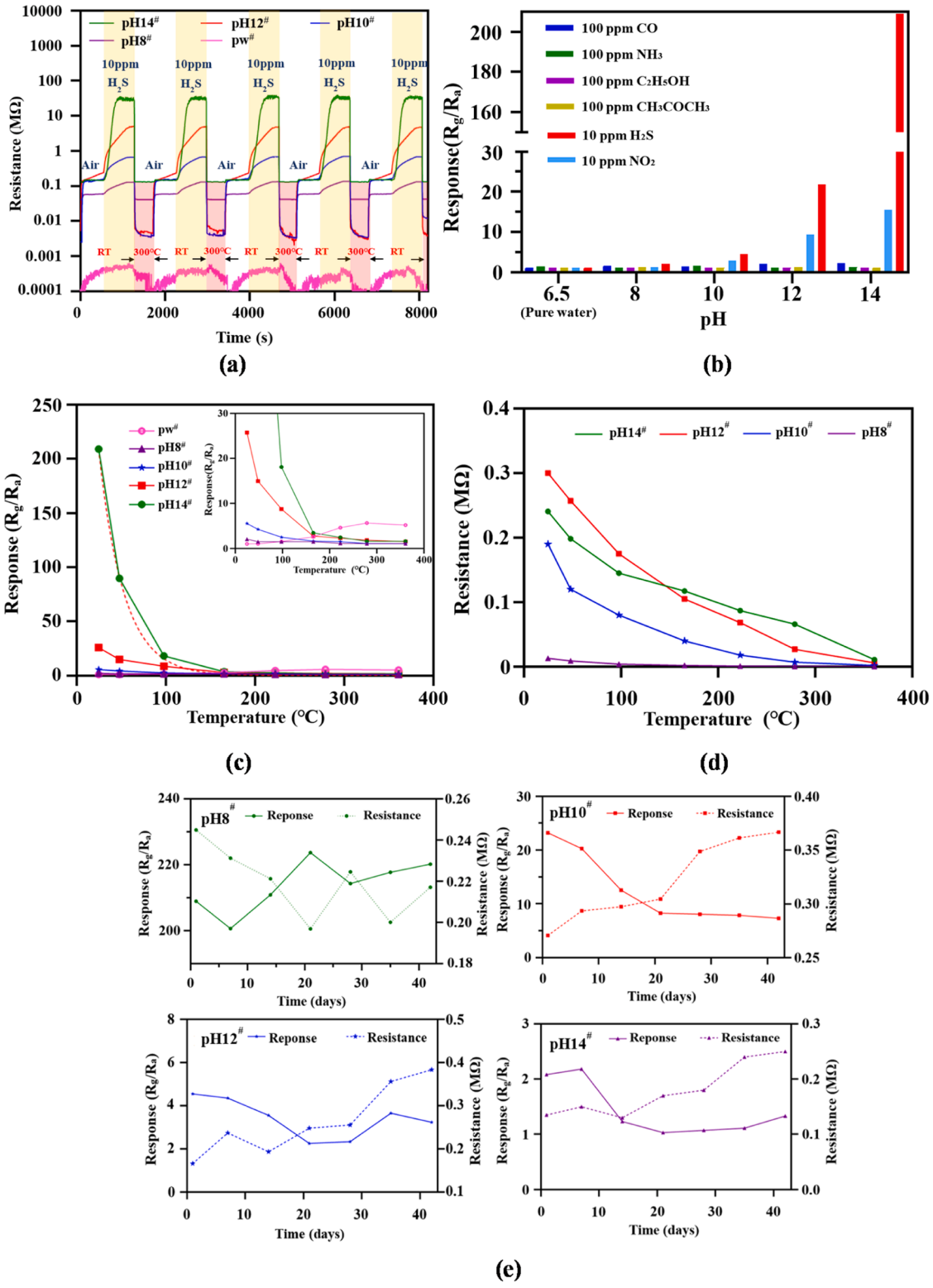

Fig. 10. (a) Response curves of the Cu_nO sensors to 10 ppm H_2S over five cycles. Response values of the Cu_nO sensors (b) to different gases at room temperature and (c) 10 ppm H_2S at different operating temperatures. (d) Baselines (R_a) of the Cu_nO nanoflowers sensors at different operating temperatures. (e) Response values and baselines (R_a) of the Cu_nO nanoflowers sensors to 10 ppm H_2S over 42 days.

fabricated using laser ablation was subsequently deduced, as schematically illustrated in Fig. 14. In the initial stage of the reaction, as CuO target continuously absorbed laser pulse energy, a plasma plume was generated at the interface of CuO target and liquid. This plume contained numerous neutral Cu and O atoms; Cu^{+}, Cu^{2+}, and O^{2-} ions, and electrons from the target, as indicated in formula (1) (Fig. 14 (a) [45].

Furthermore, the high temperature of the plasma plume continuously generated vaporizing species, contributing to the formation of cavitation bubbles on the surface of target [46].

When the bubbles collapsed, numerous particles were released into the pure water or NaOH solution (Fig. 14 (b)). The generated Cu^{n+} ions then reacted with OH^{-} ions, as indicated in formula (2), to form Cu

$$CuO\ (target) \xrightarrow{laser\ ablation} plasma\ \{Cu\ (atom) + O\ (atom) + Cu^{+} + Cu^{2+} + O^{-} + e^{-} \ldots\} \quad (1)$$

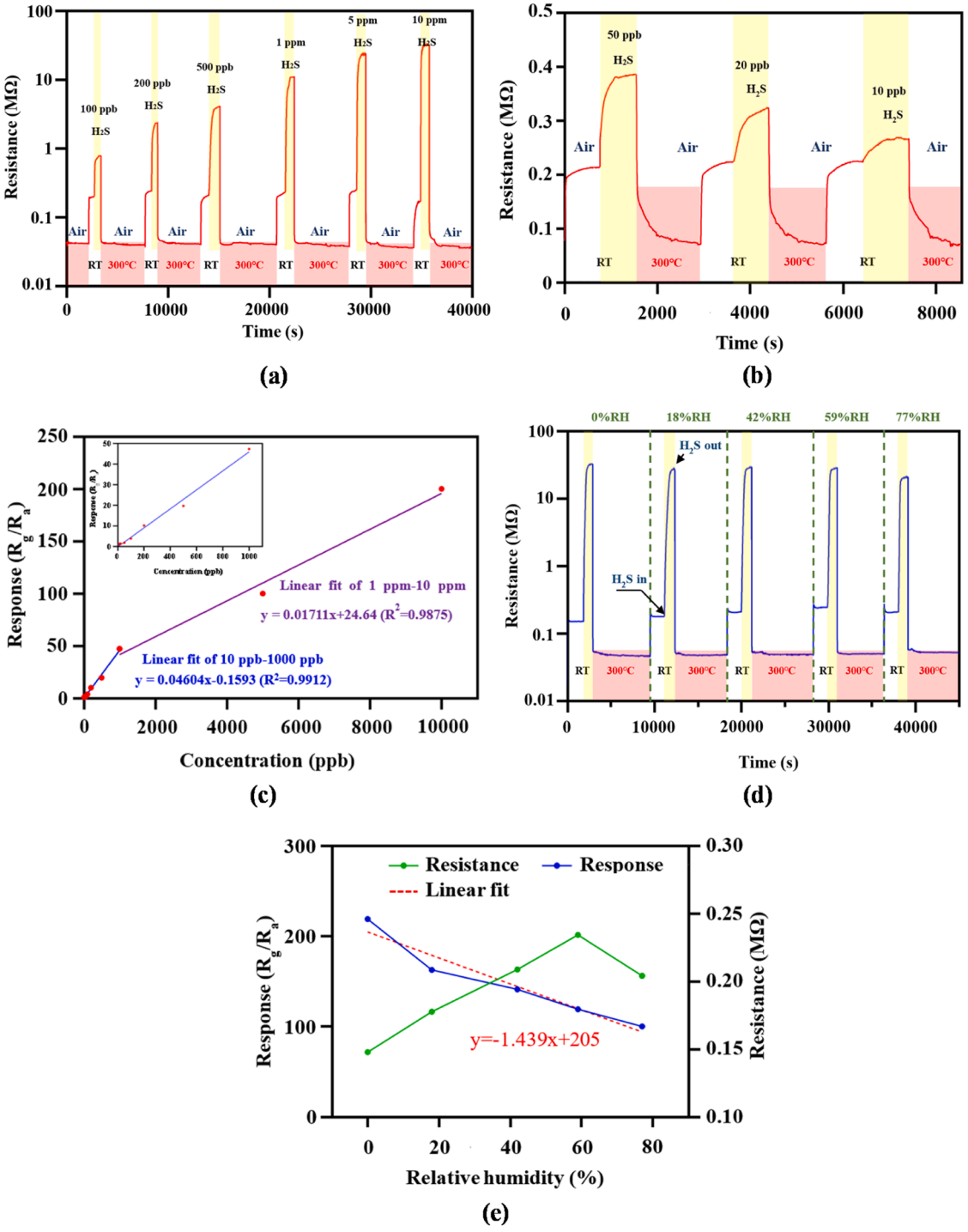

Fig. 11. (a) Response curve of the pH14# sensor to 0.1–10 ppm H_2S and (b) 10–50 ppb H_2S. (c) Linear relationship between the response value of the pH14# sensor and the concentration of H_2S. (d) Response curves, (e) response values, and baseline (R_a) of the pH14# sensor to 10 ppm H_2S under different RH conditions.

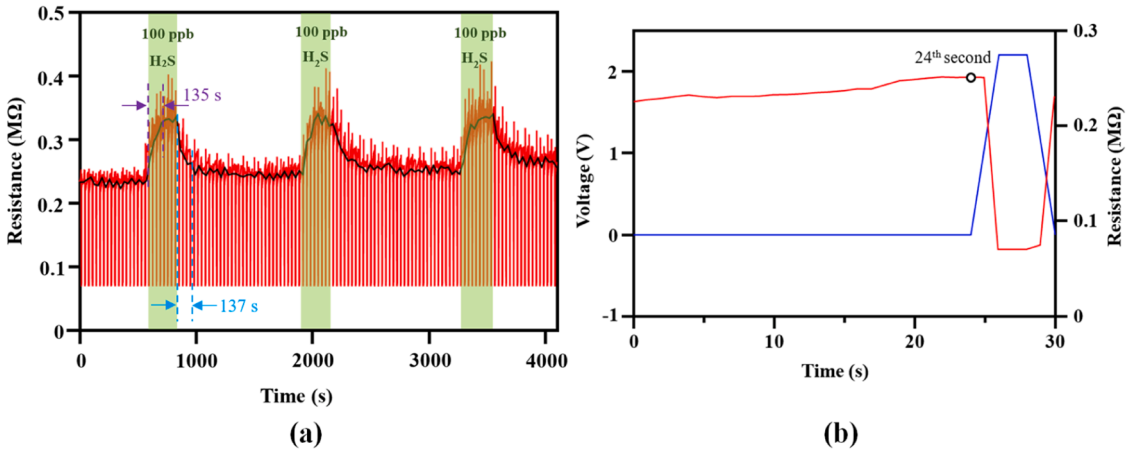

Fig. 12. (a) Response signal of pH14# to 100 ppb H_2S under pulse heating. (b) Waveform of the heating pulse and resistance of the sensor in a heating cycle.

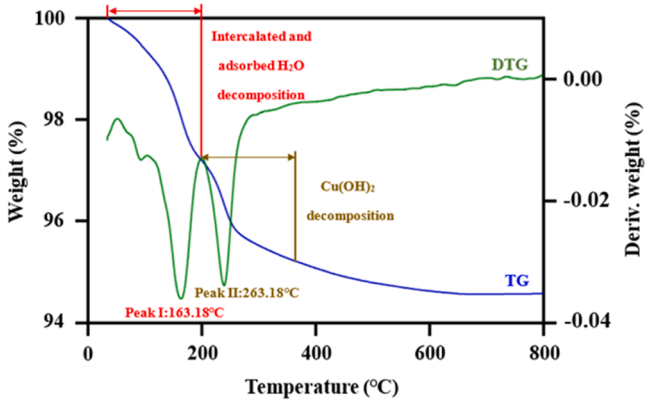

Fig. 13. TGA curve of the unannealed pH14# sample.

$(OH)_n$, which subsequently dehydrated according to formula (3) under continuous pulsed ablation treatment. Thus, the formation and dehydration of $Cu(OH)_n$ proceeded alternately, resulting in the formation of cores containing Cu_nO and $Cu(OH)_n$ (Fig. 14 (c)).

$$Cu^{n+} + OH^- \rightarrow Cu(OH)_n\downarrow \quad (2)$$

$$Cu(OH)_n \xrightarrow{laser} Cu_nO + H_2O \quad (3)$$

These cores continued to grow in the liquid. In pure water, the surfaces attracted OH^- and Cu^{n+} to form nanospindles (pw#) without interference. However, in NaOH solutions, excess OH^- ions neutralized a portion of the positive charge of Cu^{n+}, disrupting the electric neutrality on the surfaces of the cores. This impact led to the self-aggregation of the generated cores into a flower-like structure (Fig. 14 (d)) [47–49]. Finally, $Cu_nO/Cu(OH)_n$ nanoflowers were annealed at 600 °C to completely convert $Cu(OH)_n$ into Cu_nO with H_2O removal (Fig. 14 (e)).

3.3.3. Effects of high NaOH concentrations

In addition to its effect on core aggregation, highly concentrated OH^- can also react with Cu^+ according to formula (4) [50]. The conversion of Cu^+ to Cu^{2+} in NaOH solutions reduces the proportion of Cu^+ in Cu_nO nanoflowers with increasing NaOH concentrations. In particular, the ultrathin and porous structure of pH14# enhanced the corrosive action of OH^- on Cu^+, leading to complete removal of Cu^+ from the pH14# sample, as illustrated in the XRD and XPS results (Figs. 4 and 5).

$$Cu_2O + 2OH^- + H_2O \rightarrow Cu(OH)_2 + 2e^- \quad (4)$$

Meanwhile, high concentrations of OH^- significantly affect the micro-morphology of the samples. Notably, when the quantity of OH^- is considerably higher than that of Cu^{2+}, soluble $[Cu(OH)_4]^{2-}$ ions preferentially form in the presence of high NaOH concentrations, according to formula (5). Further the decomposition of $[Cu(OH)_4]^{2-}$ according to formula (6) leads to the growth of $Cu(OH)_2$ along the coordination self-assembly direction of quadrilateral $[Cu(OH)_4]^{2-}$ ions, resulting in 2D layered nanostructures [27,51]. This process contributes to the thinning and lengthening of the petals of the nanoflowers. Hence, the high ratio of OH^- to Cu^{2+} ions in the NaOH solution with a pH of 14 likely results in the ultrathin structure of the pH14# sample with a large specific surface area, as shown in the SEM results (Fig. 6).

$$Cu^{2+} + OH^- \rightarrow [Cu(OH)_4]^{2-} \quad (5)$$

$$[Cu(OH)_4]^{2-} \rightarrow Cu(OH)_2\downarrow + OH^- \quad (6)$$

3.4. Gas-sensing mechanism

To confirm the adsorption of H_2S on the Cu_nO nanoflowers, the mass change of pH14# during H_2S sensing was measured, and the result is depicted in Fig. 15. The gas flow velocity was maintained at 5 sccm throughout the measurement. After air flowed through the chamber, the processes of gas molecule adsorption and desorption gradually achieved equilibrium on the pH14# sample, and the corresponding stable weight was defined as a baseline to quantify the mass change. As 10 ppm H_2S flowed through the chamber, the mass of pH14# increased immediately, corresponding to the adsorption of H_2S on its surface. Then when the chamber was full with pure air again, mass loss occurred at once, indicating that H_2S was gradually desorbed from the surface. However, the mass of the sample remained at 393 pg instead of recovering to zero, which indicates the presence of residues on the sample. Subsequently, the pH14# sample was heated to 300 °C in 60 s. Its mass decreased rapidly at 300 °C and continued to decline after reaching zero, attributed to the desorption of both H_2S and O_2. This result confirms that H_2S was adsorbed on the surface of the sample and its byproducts did not completely desorb at room temperature; hence, high-temperature cleaning is necessary and effective for the recovery of pH14# sensors.

Fig. 16 depicts the H_2S sensing mechanism model of the Cu_nO nanoflower sensors. Cu_2O and CuO are known to exhibit p-type characteristics owing to the presence of Cu vacancies, with holes serving as the major charge carriers. In air atmosphere, substantial amounts of oxygen species are adsorbed on the surfaces of the Cu_nO nanoflowers, and a transition from physisorption to chemisorption occurs subsequently, predominantly converting oxygen to O_2^- at room temperature, as depicted in Fig. 16 (b) [40,52].

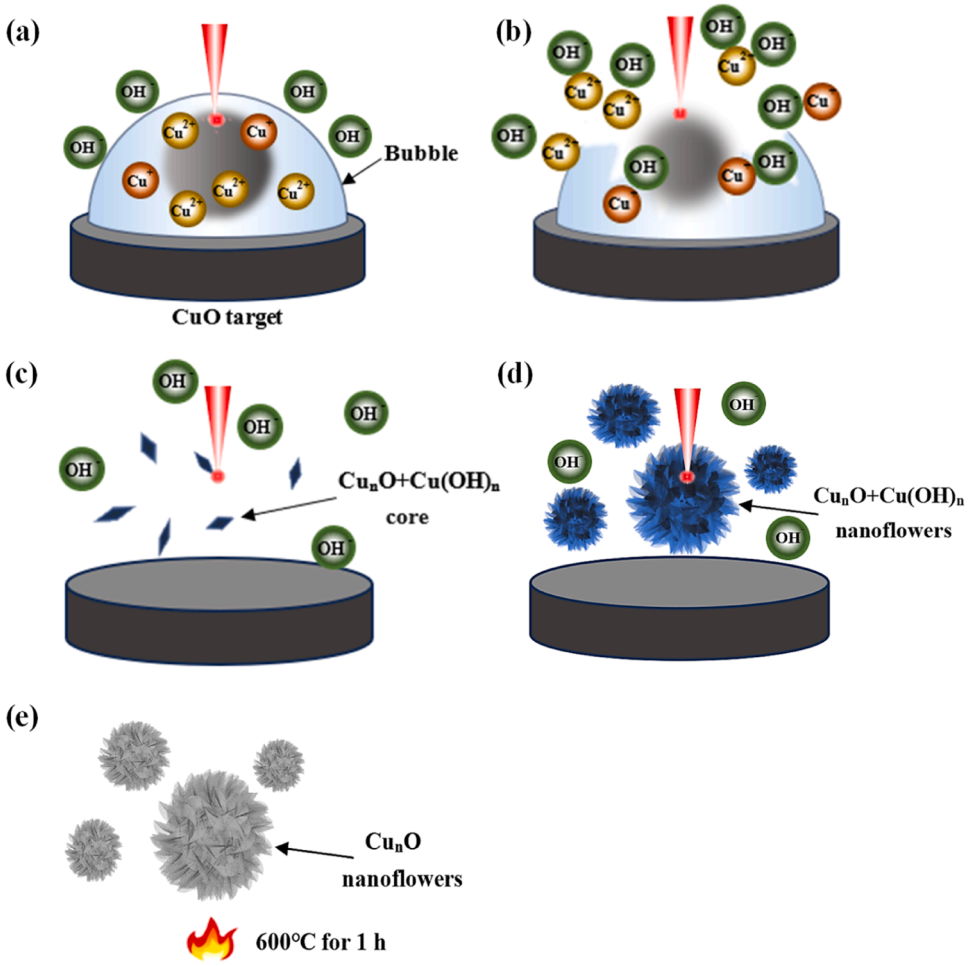

Fig. 14. Growth mechanism of Cu_nO nanoflowers. (a) Generation of Cu^+, Cu^{2+}, and cavitation bubbles, (b) contact of Cu^+ and Cu^{2+} with OH^- after bubble collapse, (c) generation of $Cu_nO/Cu(OH)_n$ cores, (d) generation of $Cu_nO/Cu(OH)_n$ nanoflowers, and (e) generation of Cu_nO nanoflowers after dehydration.

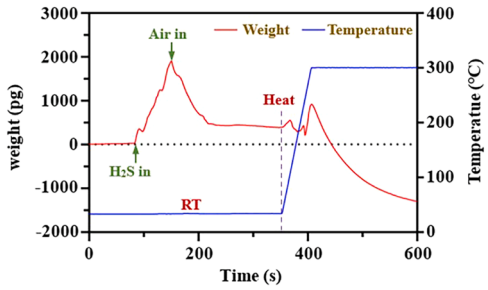

Fig. 15. Mass change of pH14# during 10 ppm H_2S sensing.

$$O_2 \quad (gas) \rightarrow O_2\ (ads) \tag{7}$$

$$O_2 \quad (ads) + e^- \rightarrow O_2^- \quad (ads)\ (T < 100℃) \tag{8}$$

For Cu_2O or CuO, the chemical bonding between Cu and adsorbed oxygen results in the transfer of the valence electrons from the sensing material to the adsorbed oxygen species, thus creating a hole accumulation layer at the interface, resulting in a small resistance.

As a strong reducing gas, H_2S can react with O_2^- according to Eq. (9), and electrons trapped by the adsorbed oxygen can return to the sensing materials, which reduces the hole accumulation layer and increases the resistance of the Cu_nO nanoflowers sensors at room temperature, as illustrated in Fig. 16 (c).

$$2H_2S + 3O_2^- \rightarrow 2SO_2 + 2H_2O + 3e^- \tag{9}$$

Furthermore, H_2S can directly react with CuO and Cu_2O to produce CuS and Cu_2S, leading to decrease in Cu_nO sensor' resistance owing to the metallic characteristics of CuS and Cu_2S. However, the response of Cu_nO sensor is opposite to the effect of sulfuration of CuO or Cu_2O on resistance; hence, the direct reaction of CuO and Cu_2O with H_2S is not the main reaction occurring on the surfaces of Cu_nO nanoflower sensors at room temperature. Nevertheless, the sulfuration of CuO and Cu_2O can be intensified at high temperatures[40,53], which could lead to reduced sensors' responses, as depicted in Fig. 10 (c).

To further explore the primary reaction occurring on the CuO nanoflowers during H_2S sensing, O 1 s and S 2p high resolution spectra of pH14# before and after exposure to 10 ppm H_2S were examined, as illustrated in Fig. 17. The as-prepared pH14# sample was characterized by XPS before exposed to H_2S. Then, this sample was sealed in a chamber filled with 10 ppm H_2S for 24 h and characterized by XPS again immediately to examine the chemical states of O and S after H_2S sensing. Fig. 17 (a) indicates that the proportion of adsorbed oxygen decreased from 64.8 % to 51.75 % after exposure. The S 2p peak is apparent in the spectrum of pH14# after exposure, with a primary peak located at approximately 168.8 eV, corresponding to the oxidation valence state of S rather than monosulfide (S^{2-}) or disulfide (S_2^{2-}) species [54]. The consumption of adsorbed oxygen and oxidation of H_2S suggest that the reaction of H_2S sensing follows formula (9).

During H_2S sensing, the porous structures of hierarchical Cu_nO nanoflowers provide abundant gas diffusion paths and large specific

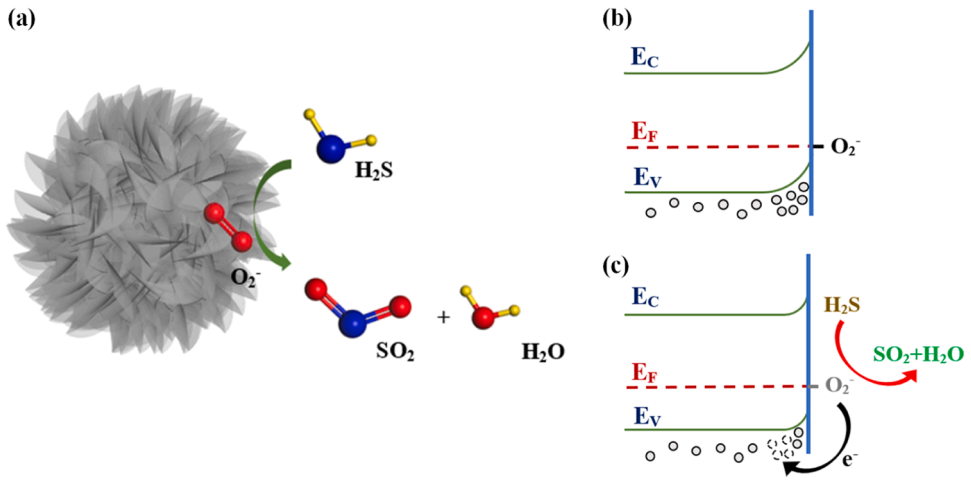

Fig. 16. H_2S sensing mechanism model of the Cu_nO nanoflower sensors. (a) Electron transfer (b) in air and (c) in H_2S.

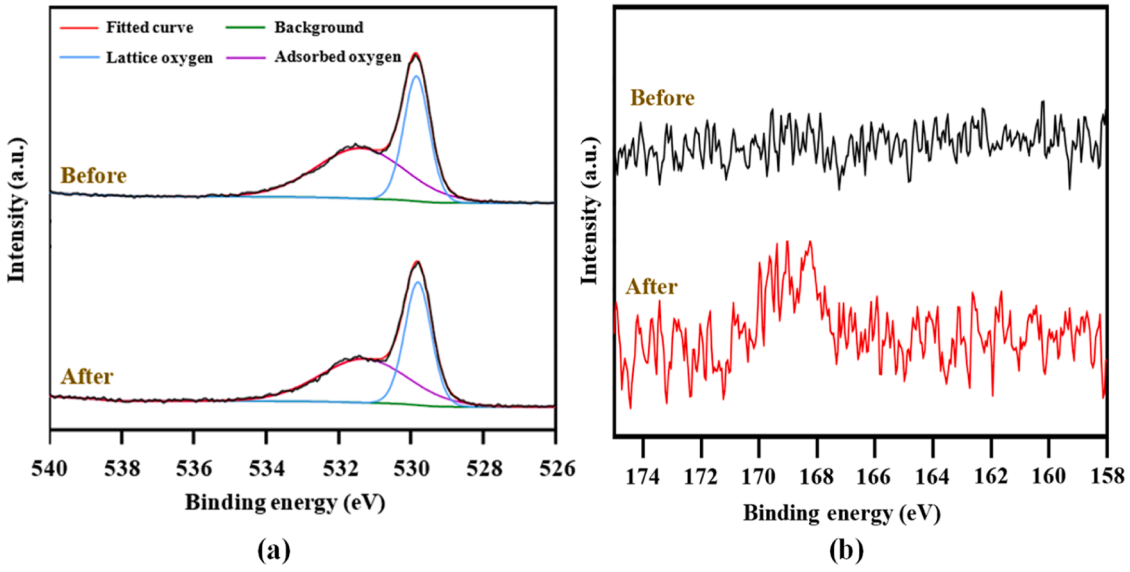

Fig. 17. (a) O 1 s and (b) S 2p high resolution spectra of pH14[#] before and after exposure to 10 ppm H_2S.

Table 1
H_2S sensing performance of recently developed CuO sensors.

CuO structure	Temperature (°C)	Concentration (ppm)	Response	Detection Limit (ppb)	τ_{res}/ τ_{rec} (s)	Ref.
Nanoneedle	150	10	76	161*	92/196	[19]
Nanoparticles	40	0.2	2.9	200	49/-	[58]
	heating pulse (350 °C, 30 s)				49/124	
Microspheres	180	100	46	100	18/42.5	[59]
Porous Films	325	1.5	2.7	150	2.7/514	[60]
Microflowers	RT	1	2.1	100	240/1341	[26]
Nanosheets	RT	0.2	5.01	10	336/543	[27]
Nanoarrays	RT	0.005	24.08	1.52	102/539	[61]
Microflowers	RT	1	9.92	50	128/-	[28]
	heating pulse (300 °C, 10 s)				128/130	
Nanoparticles	RT	0.01	20	0.1	200/1000	[62]
Nanoflowers	RT	0.1	2.85	10	250/-	This work
	Pulse heating (300 °C, 3 s in 30 s)				135/137	

RT= room temperature, τ_{res}= response time, τ_{rec}= recovery time
* Calculated theoretical detection limit.

surface areas, which improves gas response kinetics at room temperature [55]. The pH14# has the largest specific surface area among all samples, suggesting more active site available for O_2 and H_2S molecule on the pH14#, which may lead to enhanced sensitivity of pH14#. Additionally, the dramatically improved sensitivity of pH14# to H_2S may also relate to its ultrathin petals with a thickness of approximately 10 nm (Fig. 6), which is comparable to the Debye length; hence, most of the atoms can be involved in the gas-sensing reactions [56,57], thus significantly improving the sensitivity of the sensor. Simultaneously, pH14# exhibits excellent selectivity and stability likely owing to the removal of Cu_2O.

A comparison of previously reported H_2S sensors featuring various CuO nanostructures with our sensor is presented in Table 1. The table suggests that the hierarchical CuO nanoflowers in our work exhibit low detection limits at room temperature and offer fast response and recovery under pulse heating.

4. Conclusion

Hierarchical CuO nanoflowers (pH14#) comprising ultrathin nanosheets were synthesized through the laser ablation of a CuO target in NaOH solution with pH value of 14. The resulting sensor exhibited excellent sensitivity, a low detection limit, superior selectivity, and good stability. Using MHP processing pulse heating allowed the pH14# sensor to achieve response time of 135 s and recovery time of 137 s for 100 ppb H_2S. The optimal sensing performance of pH14# sensor is attributed to its large specific surface area, ultrathin thickness of its petals, and the removal of Cu_2O. These characteristics can be controlled by the concentration of NaOH in the laser ablation process. During the growth of Cu_nO nanoflowers, high concentrations of OH^- significantly influenced the specific surface area of Cu_nO nanoflowers by causing cores to self-aggregate into flower-like structures and inducing the formation of quadrilateral $[Cu(OH)_4]^{2-}$ ions. Meanwhile, high concentrations of OH^- decreased the content of Cu_2O in samples. Thus, high concentrations of OH^- can improve the H_2S sensing performance of Cu_nO products. In this study, laser ablation of a CuO target in NaOH solution was successfully utilized as a simple, green, and controlled process to obtain multiple Cu_nO nanoflowers, providing a novel synthesis method for room temperature H_2S sensitive materials.

CRediT authorship contribution statement

Guanyu Yao: Supervision, Software, Investigation, Data curation. **Jun Yu:** Supervision, Resources, Project administration, Investigation, Funding acquisition, Conceptualization. **Wenqing Zhao:** Writing – review & editing, Writing – original draft, Visualization, Validation, Software, Project administration, Methodology, Investigation, Formal analysis, Data curation. **Zhengxing Huang:** Supervision, Project administration, Conceptualization. **Huichao Zhu:** Methodology, Conceptualization. **Yadong Liu:** Software, Data curation. **Hao Wu:** Supervision, Software, Conceptualization. **Jingtong Na:** Supervision, Investigation, Conceptualization. **Xiaogan Li:** Supervision, Project administration, Formal analysis, Conceptualization. **Hongxu Liu:** Resources, Investigation, Funding acquisition, Conceptualization. **Wei Chen:** Software, Formal analysis. **Kairong Qin:** Resources, Project administration, Formal analysis, Conceptualization.

Declaration of Competing Interest

The authors declare that they have no known competing financial interests or personal relationships that could have appeared to influence the work reported in this paper.

Data availability

Data will be made available on request.

Acknowledgments

This study was financially supported by the National Key R&D Program of China (No. 2021YFB3201302), National Natural Science Foundation of China (No. 61874018), Fundamental Research Funds for the Central Universities (No. DUT22YG105) and Medical-Engineering Cross Research Fund between Liaoning Cancer Hospital & Dalian University of Technology (No. LD202206). The processing and manufacturing of MHPs were provided by Silex Microsystems Technology Co., Ltd.

Appendix A. Supporting information

Supplementary data associated with this article can be found in the online version at doi:10.1016/j.snb.2024.136732.

References

[1] M.A. Muñoz-Vargas, S. González-Gordo, J.M. Palma, F.J. Corpas, H_2S in horticultural plants: endogenous detection by an electrochemical sensor, emission by a gas detector, and its correlation with L-cysteine desulfhydrase (LCD) activity, Int. J. Mol. Sci. 23 (2022), https://doi.org/10.3390/ijms23105648.
[2] Z. Zhao, D. Cai, J. Liu, G. Zou, Q. Zhang, Z. Song, et al., H_2S cracking to produce H_2 through microwave discharge catalysis of graphitized petroleum coke, Chem. Eng. J. 476 (2023) 146711, https://doi.org/10.1016/j.cej.2023.146711.
[3] M.M. Asad, R. Bin Hassan, F. Sherwani, Q.M. Soomro, S. Sohu, M.T. Lakhiar, et al., Oil and Gas Disasters and Industrial Hazards Associated with Drilling Operation: An Extensive Literature Review, ICOMET (2019), https://doi.org/10.1109/icomet.2019.8673516.
[4] Y.H. Chan, S.S.M. Lock, M.K. Wong, C.L. Yiin, A.C.M. Loy, et al., A state-of-the-art review on capture and separation of hazardous hydrogen sulfide (H_2S): Recent advances, challenges and outlook, Environ. Pollut. 314 (2022) 120219, https://doi.org/10.1016/j.envpol.2022.120219.
[5] M. Kaur, N. Jain, K. Sharma, S. Bhattacharya, M. Roy, A.K. Tyagi, et al., Room-temperature H_2S gas sensing at ppb level by single crystal In_2O_3 whiskers, Sens. ACTUAT B-CHEM 133 (2008) 456–461, https://doi.org/10.1016/j.snb.2008.03.003.
[6] S.L. Malone Rubright, L.L. Pearce, J. Peterson, Environmental toxicology of hydrogen sulfide, NITRIC OXIDE-BIOL CH 71 (2017) 1–13, https://doi.org/10.1016/j.niox.2017.09.011.
[7] S.-W. Kang, Y.-H. Lee, Y.J. Ahn, Detection of cysteine-induced salivary H_2S to evaluate the H_2S-producing capability of oral bacteria, using a simple and sensitive colorimetric assay: A preliminary study, Microchem. J. 195 (2023) 109391, https://doi.org/10.1016/j.microc.2023.109391.
[8] M. Medani, D. Collins, N.G. Docherty, A.W. Baird, P.R. O'Connell, D.C. Winter, Emerging role of hydrogen sulfide in colonic physiology and pathophysiology, Inflamm. Bowel Dis. 17 (2011) 1620–1625, https://doi.org/10.1002/ibd.21528.
[9] M.A.N. Tian, Y.U. Wang, Y.-Q. Lu, M. Yan, Y.-H. Jiang, D.-Y. Zhao, Correlation between serum H_2S and pulmonary function in children with bronchial asthma, Mol. Med. Rep. 6 (2012) 335–338, https://doi.org/10.3892/mmr.2012.904.
[10] A.M.W.T. van den Broek, A review of the current literature on aetiology and measurement methods of halitosis, J. Dent. 35 (2007) 627–635, https://doi.org/10.1016/j.jdent.2007.04.009.
[11] P. Zuo, R. Wang, F. Li, F. Wu, G. Xu, A trace ppb-level electrochemical H_2S sensor based on ultrathin Pt nanotubes, Talanta 233 (2021) 122539, https://doi.org/10.1016/j.talanta.2021.122539.
[12] L. Lv, W. Luo, A novel ratiometric fluorescent probe for selective detection and imaging of H_2S, Spectrochim. Acta, A 246 (2021) 118959, https://doi.org/10.1016/j.saa.2020.118959.
[13] J. Che, J. Wang, C. Qiao, Y. Xia, K. Ou, J. Zhou, et al., Si-Cu nanocomposite as an effective sensing layer for H_2S based on quartz surface acoustic wave sensors, Sens. ACTUAT A-PHYS 353 (2023) 114225, https://doi.org/10.1016/j.sna.2023.114225.
[14] G. Mamtmin, N. Kari, R. Abdurahman, P. Nizamidin, A. Yimit, 5, 10, 15, 20-tetrakis-(4-methoxyphenyl) porphyrin film/K+ ion-exchanged optical waveguide gas sensor, OPT LASER TECHNOL 128 (2020) 106260, https://doi.org/10.1016/j.optlastec.2020.106260.
[15] Q. Zhou, L. Yang, Z. Kan, J. Lyu, M. Xuan Wang, B. Dong, et al., Diverse scenarios selective perception of H_2S via cobalt sensitized MOF filter membrane coated Three-Dimensional metal oxide sensor, Chem. Eng. J. 450 (2022) 138014, https://doi.org/10.1016/j.cej.2022.138014.
[16] A. Kumar, A.K. Shringi, M. Kumar, RF sputtered CuO anchored SnO_2 for H_2S gas sensor, Sens. ACTUAT B-CHEM 370 (2022) 132417, https://doi.org/10.1016/j.snb.2022.132417.
[17] P.H. Phuoc, C.M. Hung, N. Van Toan, N. Van Duy, N.D. Hoa, N. Van Hieu, One-step fabrication of SnO_2 porous nanofiber gas sensors for sub-ppm H_2S detection, Sens. ACTUAT A-PHYS 303 (2020) 111722, https://doi.org/10.1016/j.sna.2019.111722.
[18] U.T. Nakate, Y.-T. Yu, S. Park, Hydrothermal synthesis of ZnO nanoflakes composed of fine nanoparticles for H_2S gas sensing application, Ceram. Int. 48 (2022) 28822–28829, https://doi.org/10.1016/j.ceramint.2022.03.017.

[19] Q. Hu, W. Zhang, X. Wang, Q. Wang, B. Huang, Y. Li, et al., Binder-free CuO nanoneedle arrays based tube-type sensor for H_2S gas sensing, Sens. ACTUAT B-CHEM 326 (2021) 128993, https://doi.org/10.1016/j.snb.2020.128993.
[20] J. Tang, H. Wang, X. Wang, C. Xie, D. Zeng, Prussian blue-derived hollow cubic α-Fe_2O_3 for highly sensitive room temperature detection of H_2S, Sens. ACTUAT B-CHEM 351 (2022) 130954, https://doi.org/10.1016/j.snb.2021.130954.
[21] X. San, Y. Lu, G. Wang, D. Meng, X. Gong, Q. Jin, In situ growth of WO_3 nanotube arrays and their H_2S gas sensing properties for reduced operating temperature, Mater. Lett. 271 (2020) 127716, https://doi.org/10.1016/j.matlet.2020.127716.
[22] Y. Sun, J. Cui, C. Wang, S. Fu, S. Sun, X. Wang, Controllable synthesis of defect-enriched MoO_3 for enhanced H_2S sensing through hydrothermal methods: Experiments and DFT calculations, J. Alloy. Compd. 968 (2023) 172035, https://doi.org/10.1016/j.jallcom.2023.172035.
[23] C. Zheng, H. Zhao, Interaction mechanism among CO, H_2S and CuO oxygen carrier in chemical looping combustion: A density functional theory calculation study, Proc. Combust. Inst. 38 (2021) 5281–5288, https://doi.org/10.1016/j.proci.2020.06.260.
[24] H.-J. Kim, J.-H. Lee, Highly sensitive and selective gas sensors using p-type oxide semiconductors: Overview, Sens. ACTUAT B-CHEM 192 (2014) 607–627, https://doi.org/10.1016/j.snb.2013.11.005.
[25] M. Censabella, V. Iacono, A. Scandurra, K. Moulaee, G. Neri, F. Ruffino, et al., Low temperature detection of nitric oxide by CuO nanoparticles synthesized by pulsed laser ablation, Sens. Actuat B-CHEM 358 (2022) 131489, https://doi.org/10.1016/j.snb.2022.131489.
[26] Z. Li, J. Wang, N. Wang, S. Yan, W. Liu, Y.Q. Fu, et al., Hydrothermal synthesis of hierarchically flower-like CuO nanostructures with porous nanosheets for excellent H_2S sensing, J. Alloy. Compd. 725 (2017) 1136–1143, https://doi.org/10.1016/j.jallcom.2017.07.218.
[27] Z. Li, N. Wang, Z. Lin, J. Wang, W. Liu, K. Sun, et al., Room-Temperature High-Performance H_2S Sensor Based on Porous CuO Nanosheets Prepared by Hydrothermal Method, ACS Appl. Mater. Interfaces 8 (2016) 20962–20968, https://doi.org/10.1021/acsami.6b02893.
[28] K. Wu, C. Zhang, Facile synthesis and ppb-level H_2S sensing performance of hierarchical CuO microflowers assembled with nano-spindles, J. Mater. Sci.-Mater. EL 31 (2020) 7937–7945, https://doi.org/10.1007/s10854-020-03332-8.
[29] F. Zhang, A. Zhu, Y. Luo, Y. Tian, J. Yang, Y. Qin, CuO Nanosheets for Sensitive and Selective Determination of H_2S with High Recovery Ability, J. Phys. Chem. C. 114 (2010) 19214–19219, https://doi.org/10.1021/jp106098z.
[30] V. Amendola, D. Amans, Y. Ishikawa, N. Koshizaki, S. Scirè, G. Compagnini, et al., Room-Temperature Laser Synthesis in Liquid of Oxide, Metal-Oxide Core-Shells, and Doped Oxide Nanoparticles, Chem.-Eur. J. 26 (42) (2020) 9206, https://doi.org/10.1002/chem.202000686.
[31] H.J. Jung, Y. Yu, M.Y. Choi, Facile Preparation of Cu_2O and CuO Nanoparticles by Pulsed Laser Ablation in NaOH Solutions of Different Concentration, Bull. Korean Chem. Soc. 36 (2015) 3–4, https://doi.org/10.1002/bkcs.10012.
[32] H. Zhang, G. Duan, Y. Li, X. Xu, Z. Dai, W. Cai, Leaf-like Tungsten Oxide Nanoplatelets Induced by Laser Ablation in Liquid and Subsequent Aging, Cryst. Growth Des. 12 (2012) 2646–2652, https://doi.org/10.1021/cg300226r.
[33] Z. Li, J. Yu, D. Dong, G. Yao, G. Wei, A. He, E-nose based on a high-integrated and low-power metal oxide gas sensor array, Sens. Actuat. B-CHEM 380 (2023) 133289, https://doi.org/10.1016/j.snb.2023.133289.
[34] H. Wu, J. Yu, Z. Li, G. Yao, R. Cao, X. Li, Microhotplate gas sensors incorporated with Al electrodes and 3D hierarchical structured PdO/PdO_2-SnO_2:Sb materials for sensitive VOC detection, Sens. Actuat. B-CHEM 329 (2021) 128984, https://doi.org/10.1016/j.snb.2020.128984.
[35] S. Park, S. An, Y. Mun, C. Lee, UV-Enhanced NO_2 Gas Sensing Properties of SnO_2-Core/ZnO-Shell Nanowires at Room Temperature, ACS Appl. Mater. Interfaces 5 (2013) 4285–4292, https://doi.org/10.1021/am400500a.
[36] H.M.A. Hassan, M.S. Alhumaimess, I.H. Alsohaimi, S.K. Mohamed, O.F. Aldosari, T. S. Alraddadi, One-pot phyto-mediated combustion technicality for synthesizing Pd adorned Cu_2O@CuO heterojunction with great efficiency in CO oxidation and epoxidation applications, Colloid Surf. A 654 (2022) 130056, https://doi.org/10.1016/j.colsurfa.2022.130056.
[37] S.K. Chawla, N. Sankarraman, J.H. Payer, Diagnostic spectra for XPS analysis of Cu O S H compounds, J. Electron. Spectrosc. Relat. Phenom. 61 (1992) 1–18, https://doi.org/10.1016/0368-2048(92)80047-C.
[38] L. Lu, X. Xu, J. Yan, F.-N. Shi, Y. Huo, Oxygen vacancy rich Cu_2O based composite material with nitrogen doped carbon as matrix for photocatalytic H_2 production and organic pollutant removal, Dalton Trans. 47 (2018) 2031–2038, https://doi.org/10.1039/C7DT03835F.
[39] B. Lin, H. Chen, W. Wei, J. Zhang, W. Zhu, Y. Zhang, et al., Enriched oxygen vacancies of copper (I) oxide particles for enhanced removal of hydrogen sulfide at room temperature, J. Environ. Chem. Eng. 11 (2023) 110113, https://doi.org/10.1016/j.jece.2023.110113.
[40] V.X. Hien, J.-L. You, K.-M. Jo, S.-Y. Kim, J.-H. Lee, J.-J. Kim, et al., H_2S-sensing properties of Cu_2O submicron-sized rods and trees synthesized by radio-frequency magnetron sputtering, Sens. Actuat. B-CHEM 202 (2014) 330–338, https://doi.org/10.1016/j.snb.2014.05.070.
[41] Y. Ran, Y. Liu, H. Sun, H. Zhang, H. Dong, Y. Yang, et al., Surface modification of cuprous oxide nanoparticles with improved chemical stability and antibacterial activity, Appl. Surf. Sci. 565 (2021) 150566, https://doi.org/10.1016/j.apsusc.2021.150566.
[42] F. Yao, P. Xu, M. Li, X. Wang, H. Jia, et al., Microreactor-Based TG–TEM Synchronous Analysis, Anal. Chem. 94 (2022) 9009–9017, https://doi.org/10.1021/acs.analchem.2c01051.
[43] Z. Shi, R. Du, C. Yu, W. Rao, C. Xu, J. Wang, Graphene oxide/$Cu(OH)_2$ composites as efficient multifunctional hosts for lithium-sulfur batteries, J. Alloy. Compd. 925 (2022) 166642, https://doi.org/10.1016/j.jallcom.2022.166642.
[44] H. Zhang, C. Liang, Z. Tian, G. Wang, W. Cai, Organization of Mn_3O_4 nanoparticles into γ-MnOOH nanowires via hydrothermal treatment of the colloids induced by laser ablation in water, Crystengcomm 13 (2011) 1063–1066, https://doi.org/10.1039/c004482b.
[45] G.W. Yang, Laser ablation in liquids: Applications in the synthesis of nanocrystals, Prog. Mater. Sci. 52 (2007) 648–698, https://doi.org/10.1016/j.pmatsci.2006.10.016.
[46] D. Amans, M. Diouf, J. Lam, G. Ledoux, C. Dujardin, Origin of the nano-carbon allotropes in pulsed laser ablation in liquids synthesis, J. Colloid Interface Sci. 489 (2017) 114–125, https://doi.org/10.1016/j.jcis.2016.08.017.
[47] Y. Chang, Controlled synthesis and. self-assembly of single-crystalline CuO nanorods and nanoribbons, Cryst. Growth Des. 4 (2004) 397–402, https://doi.org/10.1021/cg034127m.
[48] M.H. Zaman, A. Asif, G. Zainelabdin, O. Amin, M. Nur, Willander, CuO nanoflowers as an electrochemical pH sensor and the effect of pH on the growth, J. Electroanal. Chem. 662 (2011) 421–425, https://doi.org/10.1016/j.jelechem.2011.09.015.
[49] J.P. Liu, X.T. Huang, Y.Y. Li, K.M. Sulieman, X. He, F.L. Sun, Self-assembled CuO monocrystalline nanoarchitectures with controlled dimensionality and morphology, Cryst. Growth Des. 6 (2006) 1690–1696, https://doi.org/10.1021/cg060198k.
[50] P. Preechakasedkit, N. Nawaukkaratharnant, K. Teekayupak, A. Lomae, N. Ruecha, Single-preparation rGO/Cu–Cu_2O nanocomposite-modified electrode integrating NaOH immobilized polymer blend film for one-step nonenzymatic glucose detection, J. Sci.-Adv. Mater. Dev 8 (2023) 100535, https://doi.org/10.1016/j.jsamd.2023.100535.
[51] S. Xu, J. Qu, G. Wei, T. Qi, Preparation of high specific surface area $Cu(OH)_2$ nanowires/nanorods by coordinated precipitation, Guocheng Gongcheng Xuebao/Chin. J. Process Eng. 18 (2018) 1052–1060, https://doi.org/10.12034/j.issn.1009-606X.217426.
[52] R. Kou, H. He, Y. Lu, H. Wang, J. Xu, Y.-Y. Song, et al., Boosting H_2S gas sensing performance of metal oxide semiconductors at room-temperature by the electron-extracting effect of Pt nanocluster, Chem. Eng. J. 476 (2023) 146546, https://doi.org/10.1016/j.cej.2023.146546.
[53] J. Ding, D. Wang, X. Wang, X. Wang, L. Tian, Y. Zhang, et al., Tailoring responsivity with engineered porous Cu_2O hexapods architecture towards high-performance H_2S gas-sensing, J. Mater. Sci.-Mater. EL 30 (2019) 16627–16635, https://doi.org/10.1007/s10854-019-02042-0.
[54] M.E.H.N. Tehrani, H. Naderi, F. Rashchi, Electrochemical study and XPS analysis of chalcopyrite dissolution in sulfuric acid in the presence of ethylene glycol, Electrochim. Acta 369 (2021), https://doi.org/10.1016/j.electacta.2020.137663.
[55] J.-H. Lee, Gas sensors using hierarchical and hollow oxide nanostructures: Overview, Sens. Actuat. B-CHEM 140 (2009) 319–336, https://doi.org/10.1016/j.snb.2009.04.026.
[56] G. Korotcenkov, The role of morphology and crystallographic structure of metal oxides in response of conductometric-type gas sensors, Mat. Sci. Eng. R. 61 (2008) 1–39, https://doi.org/10.1016/j.mser.2008.02.001.
[57] D.R. Miller, S.A. Akbar, P.A. Morris, Nanoscale metal oxide-based heterojunctions for gas sensing: A review, Sens. ACTUAT B-CHEM 204 (2014) 250–272, https://doi.org/10.1016/j.snb.2014.07.074.
[58] F. Peng, Y. Sun, Y. Lu, W. Yu, M. Ge, J. Shi, et al., Studies on Sensing Properties and Mechanism of CuO Nanoparticles to H_2S Gas, Nanomaterials-Basel 10 (2020) 774, https://doi.org/10.3390/nano10040774.
[59] Y. Chao, H. Zhang, J. Li, A.-J. Wang, D.-C. Wang, Z. Jin, Enhanced H_2S Gas Sensing Properties of the Hierarchical CuO Hollow Microspheres, ECS J. Solid State Sci. Technol. 12 (2023) 067004, https://doi.org/10.1149/2162-8777/acdbe8.
[60] D. Jung, S. Hwang, H.-J. Kim, J.-H. Han, H.-N. Lee, Characterization of Porous CuO Films for H_2S Gas Sensors, Materials 15 (2022) 7270, https://doi.org/10.3390/ma15207270.
[61] Z. Huang, X. Wang, F. Sun, C. Fan, Y. Sun, F. Jia, et al., Super response and selectivity to H_2S at room temperature based on CuO nanomaterials prepared by seed-induced hydrothermal growth, Mater. Des. 201 (2021) 109507, https://doi.org/10.1016/j.matdes.2021.109507.
[62] D. Li, Y. Tang, D. Ao, X. Xiang, S. Wang, X. Zu, Ultra-highly sensitive and selective H_2S gas sensor based on CuO with sub-ppb detection limit, Int. J. Hydrog. Energy 44 (2019) 3985–3992, https://doi.org/10.1016/j.ijhydene.2018.12.083.

Wenqing Zhao She is currently a Ph.D. student at Dalian University of Technology. Her current research interests include gas sensing nanomaterials, microsensors and electro-hydrodynamics printing.

Guanyu Yao received the B.S. degree in electronic science and technology from Dalian University of Technology, Dalian, Liaoning, China, in 2017. He is currently a Ph.D. student at Dalian University of Technology. His current research interests include gas sensing nanomaterials, microsensors and electrohydrodynamics printing.

Hao Wu received the B.S. degree in Electronic Information Engineering and IC design from Dalian University of Technology, Dalian, China, in 2011. His current research interests include gas sensing nanomaterials, electrohydrodynamic printing, and MEMS gas sensors.

Yadong Liu He is currently a master student at Dalian University of Technology. His current research interests include microsensors and electrohydrodynamics printing.

Huichao Zhu is an associate professor in the School of Electronic Science and Technology, Dalian University of Technology, China. He received his doctoral degree from the Department of Electronic Engineering, Jilin University, China, in 2007. He has worked in the center for post-doctoral studies in Peking University from 2007 to 2009. His current scientific interests are low dimensional metal oxide semiconductor materials and devices.

Zhengxing Huang graduated from the Department of Physics, Dalian University of Technology, and received his PhD degree from the School of Telecommunication, Dalian University of Technology. His main research direction is thermal properties of materials at micro/nano scale, with emphasis on testing methods and computer simulation methods.

Wei Chen is a thoracic surgeon at Liaoning Cancer Hospital. His main research interests include the diagnosis and treatment of lung cancer, mediastinal tumors and other thoracic surgical diseases.

Xiaogan Li is a professor in the School of Microelectronics in Dalian University of Technology. He received his Ph.D. in Materials Science and Engineering from University of Leeds, U.K. and conducted a two-year postdoctoral research term in chemical gas sensors at The Ohio State University in USA. His research interest is in chemical gas sensors.

Hongxu Liu is the Vice President and Chief of Thoracic Surgery at Liaoning Provincial Tumor Hospital. His main research interests include the diagnosis and treatment of lung cancer, esophageal cancer, tracheal tumors and other diseases.

Kairong Qin is a professor at Dalian University of Technology. He received his B.S. and Ph. D. degrees from Fudan University. His research interest is on the fields of biomechanics, microfluidic chips, and intelligent medical information detection.

Jingtong Na received the Ph.D. degree in biomedical engineering from Dalian University of Technology, Dalian, Liaoning, China, in 2023. He has been engaged in full-time scientific research in the Department of Nephrology, Affiliated Central Hospital of Dalian University of Technology. His current research interests include microfluidic mechanics and microfluidic chip system.

Jun Yu received the Ph.D. degree in mechanical and electronic engineering from Dalian University of Technology, Dalian, Liaoning, China, in 2006. She is currently an Associate Professor with Dalian University of Technology. Her current research interests include microsensors and heat transfer in micro-/nanoelectronic systems.